A Multistep Technique with Implicit Difference Schemes for Calculating Two- or Three-Dimensional Cavity Flows

KATUHIKO GODA

Toshiba Research and Development Center, Komukai, Kawasaki, 210, Japan

A numerical algorithm for solving two- or three-dimensional incompressible viscous Navier–Stokes equations is presented. The technique presented here is based on a simple variant of the Chorin method and is related to the MAC method. Auxiliary velocity fields are introduced, which are calculated by the use of a fractional-step procedure for the convective and diffusive part of the solution. For the pressure resolution, a triple sweep is used to obtain the fluid pressure. By these fractional techniques, the three-dimensional equations are separated into only one-dimensional forms. Thus, this saves more computation time and makes algorithm simple. Some numerical computations are made on flows within square and cubic cavities, and some comparisons are made in regard to boundary effects in three-dimensional flows. Further, some discussions are made on primary and secondary eddies generated in a cubic cavity, and comparisons with those in a square cavity are also made. It was found that boundary effects mainly locate near a side wall, but these are not negligibly small in a central region in a cubic cavity.

1. INTRODUCTION

A number of numerical studies [1–8] have been made of the two-dimensional viscous flow generated in a square cavity by the uniform translation of the upper surface of a cavity. This physical problem is of theoretical importance because it is a typical example of steady separated flow. From the aspect of the numerical computation, this may be a good problem to check the numerical method for solving the Navier–Stokes equation for its simple boundary conditions. In the three-dimensional case, this is also a good problem from the above viewpoint.

In this paper, a numerical method for solving the three-dimensional incompressible Navier–Stokes equation is presented, and some numerical studies are made on the flows within a cubic cavity, including a square cavity in the two-dimensional case.

A few numerical methods for solving the three-dimensional incompressible Navier–Stokes equation have been presented. Chorin [9] proposed a useful technique based on Helmholtz's decomposition theorem; any vector field A can be uniquely decomposed into its solenoidal part A_s (div $A_s = 0$) and its irrotational part A_i (rot $A_i = 0$) if the normal component of A_s on the boundary is zero. He adopted Du-Fort Frankel relaxation for the decomposition. His method is widely applicable to three-dimensional flows. Hirt and Cook [10] have made computational experiments using an ordinary

76

explicit scheme which is essentially based on Harlow and Welch [11] (so-called MAC method). Nichols and Hirt [12] have applied this to the three-dimensional free surface flow. Patanka and Spalding [13] have presented a numerical method for solving the steady three-dimensional viscous flow by a parabolic flow approximation. When the primary flow direction is dominated by an upstream condition, we can neglect its reverse flow effect and diffusion effect in the flow direction. Under these assumptions, the steady Navier–Stokes equation becomes parabolic in the flow direction. This approximation makes it possible to obtain numerical solutions by a stepwise integration in the primary flow direction from prescribed upstream initial conditions. This technique was also used by Briley [14] for three-dimensional steady flows in ducts. Takami and Kuwahara [15] have made numerical studies on the flow within a cubic cavity. They made some comparisons with the results for a square cavity obtained by Burggraf [3].

The technique presented here is based on a simple variant of the Chorin method and is essentially related to the MAC method.

In Section 2, general formulations used here are presented. An essential point in numerically solving the incompressible viscous Navier–Stokes equation is how to obtain velocity fields satisfying the divergence-free condition. Without solving a large scaled homogeneous equation generated by coupling a discretized Navier–Stokes equation with a discretized mass balance equation, it is possible to obtain the divergence-free velocity field by introducing a corrective pressure field or by treating independently with the pressure term. These two techniques are essentially the same, from the aspect of numerical analysis. Here, the latter technique was adopted, corresponding to Chorin's idea. An auxiliary velocity field is introduced, which is calculated while omitting the pressure term from the Navier–Stokes equation. Then the pressure field and the velocity field satisfying the divergence-free condition are calculated.

In Section 3, detailed numerical procedures are given, including boundary conditions. An auxiliary velocity field for the three-dimensional flow is numerically obtained, using the technique of the splitting and fractional-step methods [16]. These technique can be applied to multidimensional problems, that is, one can replace a multidimensional problem by a succession of one-dimensional ones. For the case of multidimensional heat flows, when the Crank–Nicholson scheme is used for each one-dimensional equation, unconditional stability holds [17]. This is the reason why these techniques are adopted in the present flow problem. These stability condition seems to become less severe than those of ordinal explicit difference schemes. A Poisson equation, deduced for the pressure resolution, is solved by a triple sweep, an iterative method. For boundary conditions, introducing an image fluid flow out of the boundary, it is easy to impose nonslip (antisymmetry) or slip (symmetry) conditions on the boundary. Moreover, for the pressure boundary condition, a Neumann condition can be obtained by substituting the velocity boundary conditions into the Navier–Stokes equation.

In Section 4, some numerical results for square and cubic cavities are reported. These are compared with results reported by Burggraf [3] and Takami and Kuwahara

[15]. First, numerical experiments were made on a square cavity flow for the cases of Reynolds number $R = 100$, 400, and 1000, with the aim of checking the validity of the present algorithm for the three-dimensional flow. Though Burggraf treated with the steady-state equation, with regard to stream function and vorticity, the present experiments deal with the original time-dependent Navier–Stokes equation, making straightforward calculation applicable to the three-dimensional flow. Next, computer experiments were performed for the three-dimensional flow within a cavity for Reynolds number $R = 100$ and 400. Based on results from these experiments, boundary effects were studied for cubic cavity flows. Also, secondary vortices, generated in a corner of the cavity, were studied.

2. FORMULATION

When we numerically solve the incompressible viscous Navier–Stokes equation

$$\frac{\partial u}{\partial t} + \operatorname{grad} P = -(u \operatorname{grad}) u + \frac{1}{R} \Delta u, \tag{1}$$

and the mass balance equation

$$\operatorname{div} u = 0, \tag{2}$$

using the difference method, the following two steps should be dealt with in general. Here, u is the velocity vector, P is pressure, and R is the Reynolds number. Numerical solutions for Eqs. (1) and (2) are obtained at each time step $t = n\Delta t$, according to a time increment Δt. First, an auxiliary velocity is calculated by a difference scheme approximating Eq. (1). At this stage, this velocity field does not yet satisfy mass balance relations. Second, pressure and velocity values at the next step are obtained by using a discretized mass balance equation.

Consider difference schemes of Eqs. (1) and (2):

$$\frac{1}{\Delta t}(u^{n+1} - u^n) = F\left(-(u \operatorname{grad}) u + \frac{1}{R} \Delta u\right) - GP^{n+1}, \tag{3}$$

$$Du^{n+1} = 0, \tag{4}$$

where F is a suitable difference operator (given in the next section). Symbols G and D denote difference operators corresponding to grad and div, respectively. There are two different algorithms for calculating Eqs. (3) and (4).

One method is given as follows. Taking an auxiliary velocity field $\hat{u}$ and a corrective pressure P^*, such that

$$P^{n+1} = P^n + P^*, \tag{5}$$

we have

$$\frac{1}{\varDelta t} (\hat{u} - u^n) = F\left(- (u \text{ grad}) u + \frac{1}{R} \varDelta u\right) - GP^n, \qquad (6)$$

$$\frac{1}{\varDelta t} (u^{n+1} - \hat{u}) = -GP^*. \qquad (7)$$

First, $\hat{u}$ is calculated by Eq. (6). Though $\hat{u}$ is a numerical solution approximating the Navier–Stokes Eq. (1) at $t = n \varDelta t$, it does not yet satisfy mass balance Eq. (4). Second, therefore, using Eqs. (4) and (7), we obtain the $(n + 1)$th velocity which satisfies mass balance relations, and obtain the $(n + 1)$th pressure field. That is, operating D to Eq. (7), we get

$$\frac{1}{\varDelta t} (-D\hat{u}) = -DGP^*, \qquad (8)$$

by Eq. (4). Hence, Eq. (8) becomes a discretized Poisson equation for P^*:

$$LP^* = \frac{1}{\varDelta t} D\hat{u}, \qquad (9)$$

where $L (= DG)$ is a difference operator for Laplacian. Finally, we obtain P^{n+1} and u^{n+1} by Eqs. (7) and (5). This method corresponds to that reported by Hirt and Cook [10].

The other method is given as follows. When considering an auxiliary velocity $\hat{u}$ only, the $(n + 1)$th velocity u^{n+1} is calculated in the following form:

$$\frac{1}{\varDelta t} (\hat{u} - u^n) = F\left(- (u \text{ grad}) u + \frac{1}{R} \varDelta u\right), \qquad (10)$$

$$\frac{1}{\varDelta t} (u^{n+1} - \hat{u}) = -GP^{n+1}. \qquad (11)$$

It is noted that the pressure term does not appear in Eq. (10). Though Eq. (10) is not of a momentum conservation form, it can be easily seen that Eqs. (10) and (11) are numerically consistent with Eq. (3) by eliminating the auxiliary velocity $\hat{u}$. First, the auxiliary velocity $\hat{u}$ is calculated by Eq. (10). Then, using Eqs. (11) and (4), $Du^{n+1} = D\hat{u} - \varDelta t\, DGP^{n+1} = 0$. Here, we similarly get a discretized Poisson equation for P^{n+1}:

$$LP^{n+1} = \frac{1}{\varDelta t} D\hat{u}. \qquad (12)$$

In this case, the $(n + 1)$th pressure P^{n+1} is obtained directly. Substituting P^{n+1} into Eq. (11), the $(n + 1)$th velocity u^{n+1} is obtained. This method is a simple variant of the Chorin method [9].

These two types are essentially the same. The method used in the present calculations of the two- and three-dimensional cavity flows is based on the latter type, considering numerical stability and memory storage activities which are needed for P^* in the former type. Though boundary conditions become somewhat sophisticated, these conditions can be treated simply in the cavity flow calculation (Fig. 1).
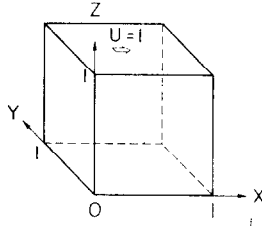

FIG. 1.   A cubic cavity.

3. NUMERICAL PROCEDURE

This section presents a numerical algorithm. First, some notations and definitions are made; $u_{i,j,k}$ ($u_{\alpha,i,j,k}, \alpha = 1, 2, 3$) represents the numerical value of velocity u at the (i, j, k) lattice point, each component is positioned at the face center of the cubic lattice; $P_{i,j,k}$ represents the numerical value of pressure P and is positioned at the body center of the cubic lattice (Fig. 2).
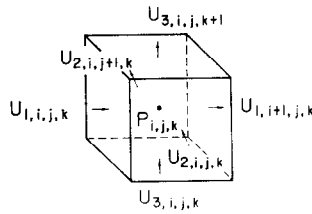

FIG. 2.   Positions for each velocity component of $u_{i,j,k}$ and pressure $P_{i,j,k}$.

Symbols δ_x and δ_{xx} denote the central differences:

$$\delta_x u = \frac{1}{2\Delta x} (u_{i+1,j,k} - u_{i-1,j,k}), \tag{13}$$

$$\delta_{xx} u = \frac{1}{(\Delta x)^2} (u_{i+1,j,k} - 2u_{i,j,k} + u_{i-1,j,k}). \tag{14}$$

Similarly, δ_y, δ_{yy}, δ_z, and δ_{zz} are defined by the central differences for each component. For the two-dimensional case, notations are given in a similar way.

3.1 *Calculation of an Auxiliary Velocity Field û*

In order to calculate an auxiliary velocity $\hat{u}$, the following scheme is adopted for Eq. (10):

$$\frac{1}{\Delta t}(u_\alpha^* - u_\alpha^n) = -u_1^n \delta_x u_\alpha^* + \frac{1}{R} \delta_{xx} u_\alpha^* = Q_x u_\alpha^*, \qquad (15)$$

$$\frac{1}{\Delta t}(u_\alpha^{**} - u_\alpha^*) = -u_2^* \delta_y u_\alpha^{**} + \frac{1}{R} \delta_{yy} u_\alpha^{**} = Q_y u_\alpha^{**}, \qquad (16)$$

$$\frac{1}{\Delta t}(\hat{u}_\alpha - u_\alpha^{**}) = -u_3^{**} \delta_z \hat{u}_\alpha + \frac{1}{R} \delta_{zz} \hat{u}_\alpha = Q_z \hat{u}_\alpha, \qquad (17)$$

where u_α^* and u_α^{**} ($\alpha = 1, 2, 3$) are new auxiliary velocities, introduced for computations. However, these variables do not need extra storage activities. This scheme is one of the splitting and fractional-step methods, which is a variant of the ADI method. Consistency of the above procedure is easily shown. Equations (15)–(17) are rewritten in the following forms, for $\alpha = 1, 2$ and 3:

$$u_\alpha^* = (1 - \Delta t \, Q_x)^{-1} u_\alpha^n,$$

$$u_\alpha^{**} = (1 - \Delta t \, Q_y)^{-1} u_\alpha^*,$$

$$\hat{u}_\alpha = (1 - \Delta t \, Q_z)^{-1} u_\alpha^{**}.$$

Eliminating the intermediate fields u_α^* and u_α^{**},

$$\hat{u}_\alpha = (1 - \Delta t \, Q_z)^{-1}(1 - \Delta t \, Q_y)^{-1}(1 - \Delta t \, Q_x)^{-1} u_\alpha^n$$

$$= (1 + \Delta t \, Q_x + \Delta t \, Q_y + \Delta t \, Q_z) u_\alpha^n + O(\Delta t^2)$$

follows. This shows that the present procedure can be said to be an approximation of Eq. (10).

Note that Eqs. (15)–(17) are of implicit form for each intermediate field u_α^*, u_α^{**}, and $\hat{u}_\alpha$. Thus, by von Neumann's linear theory [17], these schemes are unconditionally stable, assuming that each coefficient of nonlinear terms is a local constant. Though each of Eqs. (15)–(17) is independently stable, total stability condition of Eqs. (15)–(17) and Eq. (11) is not strictly derived. In numerical experiments in Section 4, however, stable solutions are obtained even if a time increment is the same order as a space increment, e.g.,

$$\Delta t \leqslant \frac{\Delta x}{|u_{max}|},$$

where u_{max} represents the maximum value of fluid velocity; $|u_{max}| = 1.0$ in the present calculations.

Boundary conditions are formally given in the following:

$$u_\alpha^* = u_\alpha^{n+1} - \Delta t(Q_y u_\alpha^{n+1} + Q_z u_\alpha^{n+1} - G_\alpha P^{n+1}), \tag{18}$$

$$u_\alpha^{**} = u_\alpha^{n+1} - \Delta t(Q_z u_\alpha^{n+1} - G_\alpha P^{n+1}), \tag{19}$$

$$\hat{u}_\alpha = u_\alpha^{n+1} + \Delta t\, G_\alpha P^{n+1}, \tag{20}$$

where G_α ($\alpha = 1, 2, 3$) denote the backward difference operator in each component, e.g.,

$$G_1 P_{i,j,k} = \frac{1}{\Delta x}(P_{i,j,k} - P_{i-1,j,k}).$$

Boundary conditions (18)–(20) are derived in the following way. In Eq. (15), an intermediate velocity field u_α^* is calculated by only the nonlinear and diffusion terms with the x-direction contribution. In order to keep numerical accuracy, this must be the same for its boundary condition. Therefore, boundary condition (18) is derived by subtracting the y- and z-direction contributions (the diffusion and nonlinear terms) and the pressure contribution from the real boundary value u_α at the $(n + 1)$th time step. In actual computation, we use an explicit form for the pressure term in Eqs. (18)–(20), i.e., the nth value P^n is used in place of the $(n + 1)$th value P^{n+1}. Moreover, in the present cavity flow calculations, since Eq. (18) is used on the $x = 0$ and $x = 1$ plane (parallel to the y-z plane), values of $Q_y u_\alpha^{n+1}$ and $Q_z u_\alpha^{n+1}$ become zero. Thus, we have

$$u_\alpha^* = u_\alpha^{n+1} + \Delta t\, G_\alpha P^n. \tag{21}$$

Equations (19) and (20) for u_α^{**} and $\hat{u}_\alpha$ are derived in a similar way, and we have finally

$$u_\alpha^{**} = u_\alpha^{n+1} + \Delta t\, G_\alpha P^n, \tag{22}$$

$$\hat{u}_\alpha = u_\alpha^{n+1} + \Delta t\, G_\alpha P^n, \tag{23}$$

where $u_1^{n+1} = 1$ on the moving wall and $u_\alpha^{n+1} = 0$ in the other cases. Detailed descriptions of these conditions are given in the next Section 3.3.

For the two-dimensional cavity flow, slightly different schemes are adopted. Auxiliary velocity fields are calculated in a straightforward manner as follows:

$$\frac{1}{\Delta t}(\hat{u}_{i,j} - u_{i,j}^n) = -u_{i,j}^n\,\delta_x u_{i,j}^n - \bar{v}_{i,j}^n\,\delta_y u_{i,j}^n + \frac{1}{R}(\delta_{xx} u_{i,j}^n + \delta_{yy} u_{i,j}^n), \tag{24}$$

$$\frac{1}{\Delta t}(\hat{v}_{i,j} - v_{i,j}^n) = -\bar{\bar{u}}_{i,j}^n\,\delta_x v_{i,j}^n - v_{i,j}^n\,\delta_y v_{i,j}^n + \frac{1}{R}(\delta_{xx} v_{i,j}^n + \delta_{yy} v_{i,j}^n), \tag{25}$$

where

$$\bar{v}_{i,j} = \tfrac{1}{4}(v_{i,j} + v_{i-1,j} + v_{i,j+1} + v_{i-1,j+1})$$

and

$$\bar{\bar{u}}_{i,j} = \tfrac{1}{4}(u_{i,j} + u_{i+1,j} + u_{i,j-1} + u_{i+1,j-1}).$$

3.2 *Pressure and Velocity Calculations at the $(n + 1)th$ Step*

Equation (12) is written in the following form:

$$\sum_{i=1}^{6} P_i^{n+1} - 6P_0^{n+1} = \frac{1}{\Delta t} D\hat{u} \qquad (= f), \tag{26}$$

where P_i represents pressure neighboring P_0 (Fig. 3). Though such a Poisson equation is solved by several algorithms, the following triple sweep was used to obtain an approximate solution. That is, for $k = 0, 1, 2,...,$

$$P_1^* - 6P_0^* + P_2^* = -P_3^{n.k} - P_4^{n.k} - P_5^{n.k} - P_6^{n.k} + f, \tag{27}$$

$$P_3^{**} - 6P_0^{**} + P_4^{**} = -P_1^* - P_2^* - P_5^* - P_6^* + f, \tag{28}$$

$$P_5^{n.k+1} - 6P_0^{n.k+1} + P_6^{n.k+1} = -P_1^{**} - P_2^{**} - P_3^{**} - P_4^{**} + f, \tag{29}$$

where $P_i^{n,0} = P_i^n$ for each i. Note that the auxiliary pressure P^* are evaluated for all the lattice points in the domain by the first sweep using Eq. (27), and so do P^{**} and $P^{n,k+1}$ for the second sweep and the third sweep, respectively. We regard the above triple sweep as one iteration. This technique is a variant of the alternative direction implicit methods for the multidimensional Poisson equation. In the present case, where the solution approaches gradually to its steady state, only one iteration may be sufficient to obtain its numerical solution, i.e., $P_i^{n+1} = P_i^{n,1}$. The $(n + 1)th$ velocity u^{n+1} is obtained by Eq. (11).
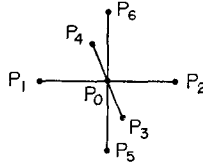

FIG. 3. Positions for pressure P_i $(i = 0, 1, 2,..., 6)$.

Here, a few remarks on the above-mentioned pressure resolution are made. Since boundary conditions for the pressure equation, which are mentioned below, can be regarded as Neumann type, we have one choice to determine an absolute value of pressure. This implies that the matrix generated by the discretized Laplacian L in Eq. (12) is not of full rank. However, it is possible to uniquely determine the pressure field by the present iteration with the prescribed initial step. Such an iteration procedure corresponds to a discrete stepwise algorithm for a parabolic equation with initial and Neumann boundary conditions. Existence and uniqueness of solutions for such a parabolic equation, with suitable conditions, are known in the theory of partial differential equation; its steady-state solution satisfies the original Poisson equation.

3.3   Initial and Boundary Conditions

For initial conditions, velocity u and pressure P are initially set to zero in the cavity.

Boundary conditions are easily imposed. Velocities on the side wall and on the bottom wall are zero, and that on the upper wall is unit velocity 1. For pressure boundary conditions, substituting the velocities on the boundary into the Navier–Stokes equation (1), we get

$$\text{grad } P = \frac{1}{R}\,\Delta u. \tag{30}$$

Therefore, when we calculate the $(n + 1)$th pressure P^{n+1} by Eq. (12), its boundary condition is approximately given by the discretized form:

$$GP^{n+1} = \frac{1}{R}\,Lu^n. \tag{31}$$

Thus, the pressure boundary condition is regarded as Neumann condition.

Here, we derive the above-mentioned boundary conditions in discrete forms. For velocity conditions, consider the reverse flow out of the fixed boundary; we call this the antisymmetry condition and also the accelerated flow out of the moving boundary, such that the velocity on the moving boundary is equal to 1.

Velocity boundary conditions used in the present cubic cavity flow are given in the following. As mentioned in the preceding section, boundary conditions for u^*, u^{**}, and $\hat{u}$ are required in the three-dimensional case.
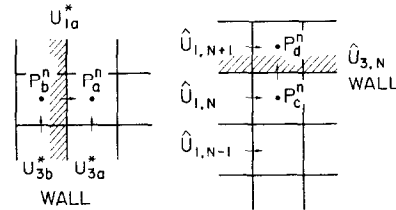
(a) A SIDE WALL   (b) A MOVING WALL

Fig. 4.   Velocity field near walls.

First, we describe boundary conditions for u^*. The auxiliary velocity u^* is calculated by Eq. (15) only in the x-direction. Therefore, boundary conditions are imposed on the $x = 0$ and $x = 1$ walls for each velocity component u_1^*, u_2^*, and u_3^*. Though $u_1^{n+1} = 0$ holds on the $x = 0$ and $x = 1$ walls, values u_1^* on these boundaries are not zero by Eq. (21), i.e.,

$$u_{1a}^* = \Delta t\, G_1 P^n$$

$$= \frac{\Delta t}{\Delta x}\,(P_a{}^n - P_b{}^n), \tag{32}$$

on the $x = 0$ wall (Fig. 4a). A similar condition is imposed on the $x = 1$ wall. For the z-component velocity u_3^*, an antisymmetry condition on both walls is imposed, for example,

$$u_{3b}^* = -u_{3a}^*, \tag{33}$$

on the $x = 0$ wall (Fig. 4a). For the y-component velocity u_2^*, the same condition is used.

Boundary conditions for u^{**} are similarly derived. The auxiliary velocity u^{**} is calculated by Eq. (16) only in the y-direction. For u_1^{**} and u_3^{**}, an antisymmetry condition is used on the $y = 0$ wall and a symmetry condition is used on the $y = \frac{1}{2}$ plane. For the y-component velocity u_2^{**}, we use the following conditions:

$$u_2^{**} = \Delta t \, G_2 P^n, \tag{34}$$

on the $y = 0$ wall, and a symmetry condition on the $y = \frac{1}{2}$ wall.

As the auxiliary velocity $\hat{u}$ is calculated in the z direction, its boundary conditions are imposed on the $z = 0$ and $z = 1$ walls. The condition used here for $\hat{u}_1$ is

$$\hat{u}_{1,N+1} = \tfrac{1}{3}(8 + \hat{u}_{1,N-1}) - 2\hat{u}_{1,N} \tag{35}$$

on the $z = 1$ wall. Each variable is shown in Fig. 4b. Equation (35) is derived by an extrapolation using the quadratic polynominal approximation satisfying the moving boundary condition (unit velocity). The condition for $\hat{u}_3$ is

$$\hat{u}_{3\,N} = \frac{\Delta t}{\Delta x} (P_d{}^n - P_e{}^n). \tag{36}$$

The condition for $\hat{u}_2$ is similar to Eq. (32). It is noted that Eq. (35) is the condition for the $(n + 1)$th step velocity u_1^{n+1}. However, in the actual computation, we approximately applied this to the calculation for the auxiliary velocity $\hat{u}_1$.

When the $(n + 1)$th velocity are obtained by Eq. (11), boundary conditions for u^{n+1} are not necessary for the calculation. If the numerical solution tends to a steady state, boundary values of u^{n+1} tend to their real boundary conditions in the present numerical procedure. For example, the auxiliary boundary value u_1^* on the $x = 0$ wall is given by Eq. (32). Since the value does not change by the u_α^{**} and u_α calculations, it still holds that

$$\hat{u}_{1a} = u_{1a}^* = \frac{\Delta t}{\Delta x} (P_a{}^n - P_b{}^n) \tag{37}$$

on the $x = 0$ wall. On the other hand, the $(n + 1)$th boundary value u_{1a}^{n+1} is obtained by Eq. (11) as follows:

$$u_{1a}^{n+1} = \hat{u}_{1a} - \Delta t \, G_1 P^{n+1}$$

$$= \hat{u}_{1a} - \frac{\Delta t}{\Delta x} (P_a^{n+1} - P_b^{n+1}). \tag{38}$$

Therefore,

$$u_{1a}^{n+1} = \frac{\Delta t}{\Delta x}\{(P_a{}^n - P_b{}^n) - (P_a^{n+1} - P_b^{n+1})\} \tag{39}$$

holds. This shows that the $(n + 1)$th boundary value tends to its real boundary value when the pressure field tends to its steady state.
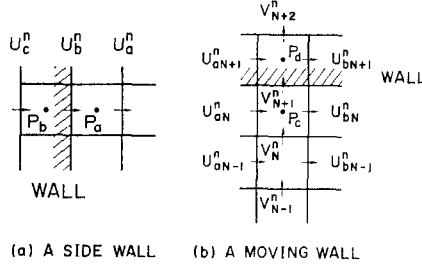

(a) A SIDE WALL　　(b) A MOVING WALL

FIG. 5.　Field variables near walls.

Pressure boundary condition (31) is used for solving the triple sweep (27)–(29). Here, we describe these conditions in discrete forms for the two-dimensional case, essentially same as for the three-dimensional case. Each variable is shown in Fig. 5. On the fixed wall, we have, from Eq. (31),

$$\frac{1}{\Delta x}(P_a - P_b) = \frac{1}{R}\frac{1}{(\Delta x)^2}(u_a{}^n - 2u_b{}^n + u_c{}^n). \tag{40}$$

Using $u_b{}^n = 0$ and $u_c{}^n = u_a{}^n$, we obtain

$$P_b = P_a - \frac{2}{R\,\Delta x}u_a{}^n. \tag{41}$$

Boundary conditions for the other fixed walls are similarly obtained. On the moving wall, we have, from Eq. (31),

$$\frac{1}{\Delta x}(P_c - P_d) = \frac{1}{R\,(\Delta x)^2}(v_{N+2}^n - 2v_{N+1}^n + v_N{}^n). \tag{42}$$

Thus by

$$v_{N+2}^n = (7/3)\,v_N{}^n - (1/3)\,v_{N-1}^n, \tag{43}$$

and by $v_{N+1}^n = 0$, we have finally

$$P_d = P_c + \frac{1}{R\,\Delta x}((10/3)\,v_N{}^n - (1/3)\,v_{N-1}^n). \tag{44}$$

Equation (43) is derived by Eq. (35) for the nth velocity u_{N+1}^n:

$$u_{N+1}^n = \tfrac{1}{3}(8 + u_{N-1}^n) - 2u_N{}^n, \tag{45}$$

and by the continuity conditions. By the continuity condition and $v_{N+1}^n = 0$, we obtain

$$v_{N+2}^n = u_{aN+1}^n - u_{bN+1}^n . \tag{46}$$

Substituting Eq. (45) into Eq. (46) for u_{aN+1}^n and u_{bN+1}^n, respectively, we obtain

$$v_{N+2}^n = \{\tfrac{1}{3}(8 + u_{aN-1}^n) - 2u_{aN}^n\} - \{\tfrac{1}{3}(8 + u_{bN-1}^n) - 2u_{bN}^n\}$$

$$= \tfrac{1}{3}(u_{aN-1}^n - u_{bN-1}^n) - 2(u_{aN}^n - u_{bN}^n). \tag{47}$$

Using the continuity conditions

$$u_{aN-1}^n - u_{bN-1}^n = v_N{}^n - v_{N-1}^n \tag{48}$$

and

$$u_{aN}^n - u_{bN}^n = -v_N{}^n \tag{49}$$

we finally get Eq. (43).

For the three-dimensional case, the same boundary conditions are used. Thus, we can continue the pressure iteration by the triple sweep.

4. RESULTS AND DISCUSSIONS

This section reports numerical results obtained for two- or three-dimensional cavity flow. First, computations for a square cavity are performed for $R = 100$, $R = 400$, and $R = 1000$. Second, computations for a cubic cavity are performed for $R = 100$ and $R = 400$.

Since the present technique for the three-dimensional calculations is essentially the same as that for the two-dimensional case, using the results for a square cavity flow, it is possible to ensure the validity of the present algorithm for a cubic cavity flow, specially treatment for boundary conditions and pressure resolution. Figures 6a and b show velocity profiles on vertical center-line of a square cavity for $R = 100$ and for $R = 400$, respectively. The present results agree well with those reported by Burggraf [3] for both cases. In Fig. 6a, a slight difference can be seen in the result for a mesh size of 1/20. It appears that a mesh size of 1/20 is still coarse for a Reynolds number of 400.

Figure 7 shows a result for a Reynolds number $R = 1000$. For such a high Reynolds number, numerical computations are not easy because of numerical stability and accuracy. However, we can obtain a satisfactory result, which almost agrees with the result obtained by Ozawa [8]. In comparing our result with that of Ozawa, however, a slight difference is seen, probably due to insufficiency of a mesh size: he used $\Delta x = 1/80$ in his calculations; the present mesh size is $\Delta x = 1/40$. For comparison, Fig. 7 also shows the result obtained by Bozeman and Dalton [7]. It seems that their result, probably obtained by the UDC method, does not yet reach the steady-state solution.
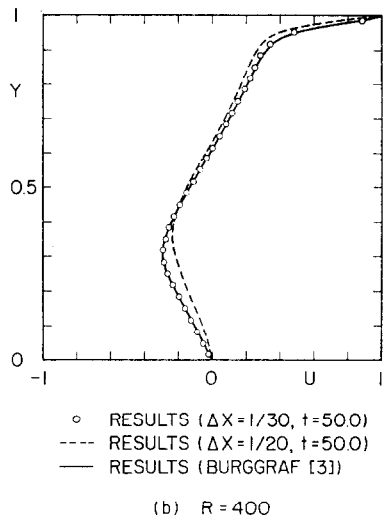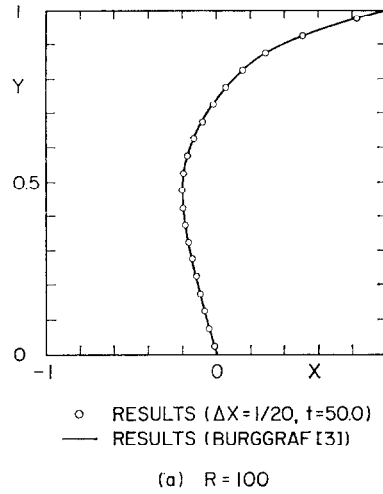
FIG. 6. Velocity profiles on vertical center-line of a square cavity: (a) $R = 100$, (b) $R = 400$.

They performed numerical computations for $R = 1000$ by two kinds of difference schemes: the UDC method and the UDD method in their notation.

A few remarks on the location of the primary vortex center and the size of the upstream corner secondary vortex are made. The computed location of the primary vortex center is $(0.538, 0.575)$ in the square cavity, expressed in Cartesian coordinates. The result by Ozawa is $(0.533, 0.529)$, and the result by Boseman and Dalton is about $(0.57, 0.575)$ which was obtained by the UDD method.

By the experimental results [18], the size of the upstream corner secondary vortex gradually increases from 0.1 to a maximum of approximately 0.35 around $R = 500$.
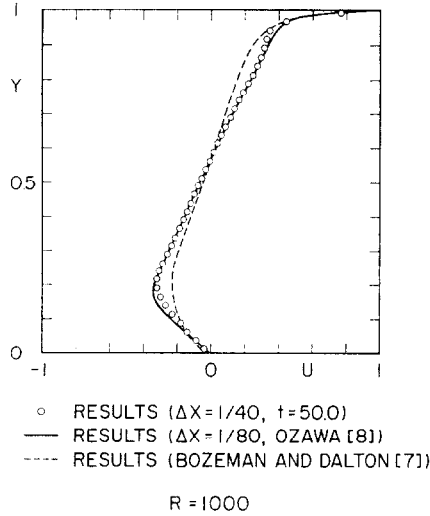
○   RESULTS (ΔX=1/40, t=50.0)
──── RESULTS (ΔX=1/80, OZAWA [8])
- - - RESULTS (BOZEMAN AND DALTON [7])

R = 1000

FIG. 7.   Velocity profiles on vertical center-line of a square cavity for $R = 1000$.

With a further increase in R, its vortex begins to shrink slowly, whose size for $R = 1000$ is about 0.27. The present computed size becomes about 0.38 for $R = 1000$. Ozawa's result is about 0.37. The size obtained by Boseman and Dalton is about 0.32. Though a decrease tendency is shown by them, these three are almost in good agreement. It can be said that these three algorithms are applicable to such a high Reynolds number.

For the three-dimensional case, the computational region dealt with is a unit cubic cavity $1 \times 1 \times 1$, whose upper boundary is the sliding wall with a unit velocity. The mesh size used here is $\Delta x = 1/20$, and the computational mesh points are reduced to $20 \times 10 \times 20$ by considering the symmetry of the cavity. In view of the results of the two-dimensional flow for the case of $R = 400$, $30 \times 15 \times 30$ mesh points are necessary to get a satisfactory result. However, it is hardly possible for such a case to perform computations because of the required computation time and memory storage activities. Thus, in this case, results for the $20 \times 10 \times 20$ lattices are compared with those of 20×20 lattices in the two-dimensional cavity. By the similar reason, we did not perform computations for a Reynolds number $R = 1000$.

Computational results for a cubic cavity flow are given in Figs. 8–12. Figure 8 shows the x-component velocity profiles on the vertical center-line of a cavity for $R = 100$. The results mostly agree with those by Takami and Kuwahara. We also give the two-dimensional results obtained by Burggraf for comparison. Figure 9 shows the results for $R = 400$. Comparing the results in a square cavity for $\Delta x = 1/20$, it is possible to observe three-dimensional boundary effects. The present results mostly agree with those reported by Takami and Kuwahara. Some comments on three-dimensional boundary effects are made below. Figure 10 shows profiles of the x-component velocity in the $x = 0.5$ plane for the cases of $R = 100$ and $R = 400$.

○   RESULTS (ΔX=1/20, t=25.0)
---- RESULTS (TAKAMI AND KUWAHARA [I5])
——   RESULTS (IN A SQUARE CAVITY,
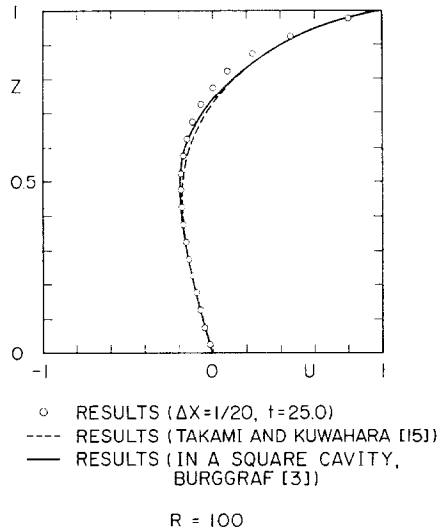   BURGGRAF [3])

R = 100

FIG. 8. Velocity profiles on vertical center-line of a cubic cavity for $R = 100$.

○   RESULTS (ΔX=1/20, t=25.0)
•   RESULTS (IN A SQUARE CAVITY, ΔX=1/20)
---- RESULTS (TAKAMI AND KUWAHARA [I5])
——   RESULTS (IN A SQUARE CAVITY,
   BURGGRAF [3])
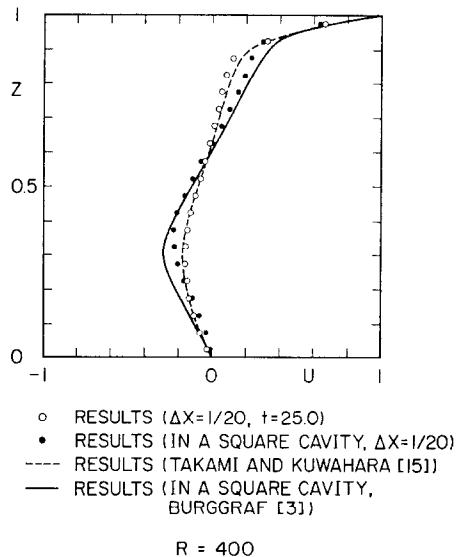
R = 400

FIG. 9. Velocity profiles on vertical center-line of a cubic cavity for $R = 400$.

For both cases, the boundary layer caused by a side wall locates near a wall. Flow patterns in the central part are almost of a two-dimensional flow. However, y-component velocity values are not so small. Table I lists their total amount, corresponding to each lattice number j, where $\sum |v|$ and $\sum v$ represent the summation of absolute values of the y-component velocity and the summation of the y-component
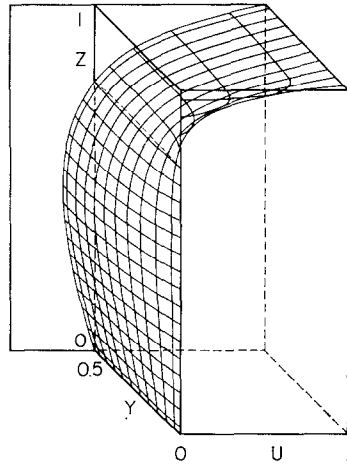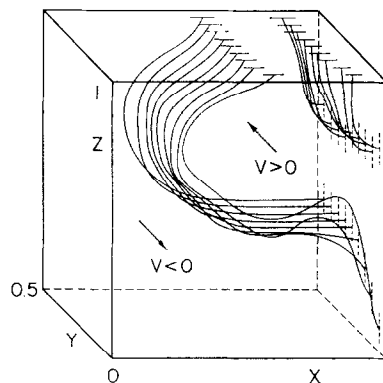
(a) R = 100
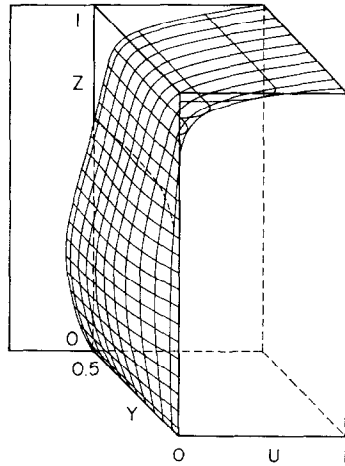
(b) R = 400

FIG. 10.   Profiles of the x-component velocity in the $x = \frac{1}{2}$ plane.

velocity values, respectively. The flow rate in the y-direction is about 2 % of that in the x- or z-direction. Figure 11 shows zero-contour lines for y-component velocities for each $y = j \, \varDelta x$ plane ($j = 1, 2,..., 9$). For both cases $R = 100$ and $R = 400$, these contours separate a cavity into two regions. One is positive velocity region and the other is negative velocity region. Even, in the central part, there is a tendency for the central flow to go toward an inner direction. On the other hand, the flow near the wall goes toward an outer direction.

TABLE I

Total Amount of y-Component Velocity in a Cavity Flow Corresponding to Each Lattice Number j

j	$R = 100$		$R = 400$	
	$\sum \lvert v \rvert$	$\sum v$	$\sum \lvert v \rvert$	$\sum v$
1	0.0	0.0	0.0	0.0
2	1.950	-0.6×10^{-7}	3.278	1.6×10^{-6}
3	3.833	0.0×10^{-6}	6.067	2.2×10^{-6}
4	5.053	-0.1×10^{-6}	7.472	3.2×10^{-6}
5	5.530	-0.1×10^{-6}	7.650	3.1×10^{-6}
6	5.381	-0.1×10^{-6}	6.980	2.7×10^{-6}
7	4.765	0.0×10^{-6}	5.780	2.1×10^{-6}
8	3.818	0.0×10^{-6}	4.377	1.3×10^{-6}
9	2.652	0.0×10^{-6}	2.916	0.6×10^{-6}
10	1.356	-0.9×10^{-6}	1.452	3.3×10^{-7}
11	0.0	0.0	0.0	0.0

Note. $j = 1$ and $j = 11$ represent the side wall and the $y = \frac{1}{2}$ plane, respectively.

(a) R = 100
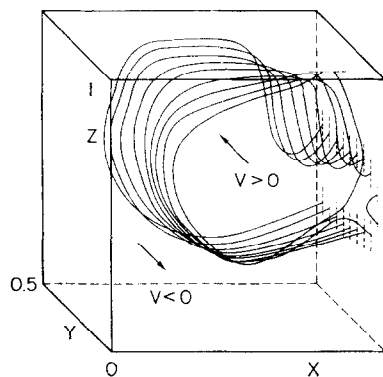
(b) R = 400

FIG. 11. Zero-contour lines of the y-component velocities for each $y = j \Delta x$ plane ($j = 1, 2, ..., 9$).
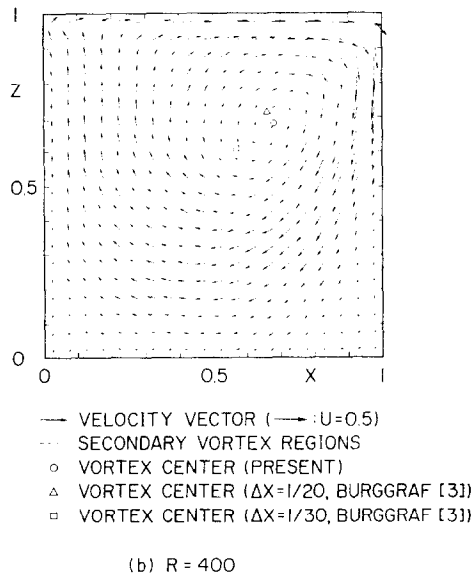
—→ VELOCITY VECTOR (—→ :U=0.5)
···· SECONDARY VORTEX REGIONS
o VORTEX CENTER (PRESENT)
△ VORTEX CENTER (ΔX=1/20, BURGGRAF [3])
□ VORTEX CENTER (ΔX=1/30, BURGGRAF [3])

(a) R = 100

—→ VELOCITY VECTOR (—→ :U=0.5)
··· SECONDARY VORTEX REGIONS
o VORTEX CENTER (PRESENT)
△ VORTEX CENTER (ΔX=1/20, BURGGRAF [3])
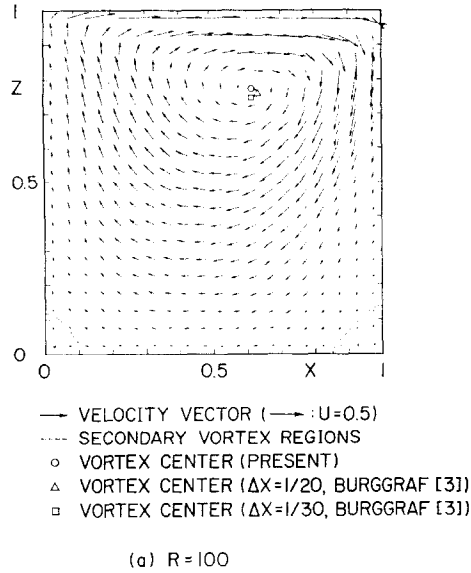□ VORTEX CENTER (ΔX=1/30, BURGGRAF [3])

(b) R = 400

FIG. 12. Profiles of the flow vector in the $y = \frac{1}{2}$ plane.

Figures 12a and b show profiles of flow vectors in the $y = \frac{1}{2}$ (strictly speaking, $y = \frac{1}{2}(1 - \frac{1}{2} \Delta x)$) plane for Reynolds numbers $R = 100$ and $R = 400$, respectively. For two-dimensional flows, its scalar stream function exists. However, since such a function does not exist in the present case, it is better to examine the structure of the flow by means of flow vectors. As shown in Figs. 12a and b, two secondary vorticies

are generated in the bottom corners in the cavity for both cases $R = 100$ and $R = 400$. Each length of the secondary eddies is almost in agreement with those reported by Burggraf in the two-dimensional case. For the primary eddy in the square cavity, Burggraf discussed mesh size dependence for the location of its center. In the present three-dimensional calculations, each location almost agrees with the results obtained by Burggraf with an accuracy of less than the mesh size $\Delta x = 1/20$ for both $R = 100$ and $R = 400$. However, these slight differences may be due to the boundary effect in the cubic cavity.
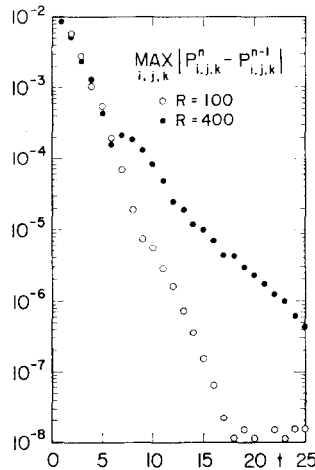

FIG. 13.   Behaviour of maximum pressure difference between two time steps.

Figure 13 shows behavior of the maximum pressure difference between two time steps: $\max | P_{i,j,k}^{n} - P_{i,j,k}^{n-1} |$. For $R = 100$, it can be said that the solution at $t = 18$ has already reached its steady state. For $R = 400$, the solution almost reaches its steady state. By numerical checking, it is found that both numerical solutions at $t = 25$ satisfy mass balance Eq. (4), with an accuracy of less than almost 10^{-6}. It is noted that the spectral radius of the iteration (24)–(26) for the Laplace equation is 0.970924.

5. CONCLUDING REMARKS

The major point of the present algorithm is to deal with only one-dimensional forms for both velocity and pressure calculations in spite of the three-dimensional equations. Further, all the schemes used here for each one-dimensional form are of implicit form. Thus, stability conditions for the present method becomes less severe. The time mesh size used in the computations is $\Delta t = 0.05$ satisfying a relation

$$\Delta t \leqslant \frac{\Delta x}{| u_{\max} |} \qquad (| u_{\max} | = 1.0),$$

which corresponds to a formal stability condition for one-dimensional hyperbolic equations. This saves more computation time and makes the algorithm simple. The present three-dimensional calculation ($R = 100$ or 400) requires 48K words and 50 min, using an ACOS-700 computer; its computation speed is about one-fourth as large as that of the CDC-6600 computer.

The numerical results show that cubic cavity flows are almost of two-dimensional form, but boundary effects are not negligibly small.

We make a remark on the velocity boundary conditions. In view of the present numerical results, though satisfactory results are obtained, it may be possible that results with high accuracy are obtained by considering the pressure correction for all the auxiliary velocity boundary conditions.

REFERENCES

1. M. KAWAGUTI, *J. Phys. Soc. Japan* **16** (1961), 2307.
2. R. D. MILLS, *J. Phys. Aeron. Soc.* **69** (1965), 714.
3. O. R. BURGGRAF, *J. Fluid Mech.* **24** (1966), 133.
4. L. M. SIMUNI, *Inzlenernü Zh.* **4** (1964), 446.
5. D. GREENSPAN, *Comput. J.* **12** (1969), 89.
6. A. K. RUNCHAL, D. B. SPALDING, AND M. WOLFSHTEIN, *Phys. Fluids Suppl. II* **12** (1969), II-21.
7. J. D. BOZEMAN AND C. DALTON, *J. Computational Phys.* **12** (1973), 348.
8. S. OZAWA, *J. Phys. Soc. Japan* **38** (1975), 889.
9. A. J. CHORIN, *Math. Comp.* **22** (1968), 745.
10. C. W. HIRT AND J. L. COOK, *J. Computational Phys.* **10** (1972), 324.
11. F. H. HARLOW AND J. E. WELCH, *Phys. Fluids* **8** (1965), 2182.
12. B. D. NICHOLS AND C. W. HIRT, *J. Computational Phys.* **12** (1973), 234.
13. S. V. PATANKA AND D. B. SPALDING, *Internat. J. Heat Mass Transfer* **15** (1972), 1787.
14. W. R. BRILEY, *J. Computational Phys.* **14** (1974), 8.
15. H. TAKAMI AND K. KUWAHARA, *J. Phys. Soc. Japan* **37** (1974), 1695.
16. A. A. SAMARSKII, *Z. Vyčisl. Mat. i Mat. Fiz.* **2** (1962), 787 or *USSR Comput. Math. and Math. Phys.* **1963** (1964), 894.
17. R. D. RICHTMYER AND K. W. MORTON, "Difference Methods for Initial-Value Problems," 2nd Ed., p. 212, Interscience, New York, 1967.
18. F. PAN AND A. ACRIVOS, *J. Fluid Mech.* **28** (1967), 643.